Nanoscale Advances

PAPER

View Article Online
View Journal

Cite this: DOI: 10.1039/d5na01101a

Sulphur-promoted growth of $Mo_6S_2I_8$ nanowires *via* a metastable $MoI_{2-x}S_x$ intermediate

Anja Pogačnik Krajnc, *[ab] Janez Jelenc, [a] Luka Pirker, [a] Srečo D. Škapin [a] and Maja Remškar [a]

Received 28th November 2025
Accepted 19th January 2026

DOI: 10.1039/d5na01101a

rsc.li/nanoscale-advances

Sulphur incorporation plays a crucial role in the formation of Mo–S–I nanostructures, but its effect on phase stability and morphology has remained unclear. Here, we show that trace sulphur stabilizes a metastable $MoI_{2-x}S_x$ phase that grows as high-aspect-ratio nanowires (NWs), in contrast to the low-aspect-ratio prisms of pure MoI_2. These intermediate NWs subsequently transform into $Mo_6S_2I_8$ NWs, revealing a sulphur-promoted growth pathway. Structural and electronic characterization using XRD, TEM, SEM, UV-Vis, Raman, UHV AFM/KPFM, and STM/STS clarifies the ambiguous role of MoI_2. The $MoI_{2-x}S_x$ NWs show diameters of 100–300 nm, lengths up to 20 μm, and a nominal composition of 7.5% S, 38% Mo, and 54.5% I. Work function measurements indicate a progressive shift from 4.6 ± 0.1 eV in the intermediate phase to 5.0 ± 0.1 eV in the final $Mo_6S_2I_8$ NWs, while density-of-states analysis reveals a U-shaped band gap of ~1.2 eV in the NW cores. Our results establish a general concept: minor compositional tuning can stabilize metastable intermediates as templates for controlled nanowire morphology and function, opening pathways for optoelectronic, nanoelectronic, and composite applications.

1. Introduction

Low-dimensional molybdenum chalcogenide–halide compounds are gaining attention for their tunable electronic, optical, and structural properties, making them promising candidates for nanoelectronics, optoelectronics, and functional composites.[1–7] Among these, Mo–S–I materials stand out due to their diverse structures, yet their synthesis remains challenging: multiple phases often form under similar conditions, hindering phase purity and morphology control.[8–14] As a result, progress in this field has been limited by an incomplete understanding of how intermediate phases influence nanostructure growth.

A particularly relevant case is molybdenum diiodide (MoI_2), a black, air-stable Chevrel-phase compound with a $[Mo_6I_8]$ cluster structure and orthorhombic symmetry.[15,16] MoI_2 is typically viewed as a by-product in chemical transport reactions,[17] which negatively impacts the yield of the $Mo_xS_yI_z$ nanowires. However, recently MoI_2 has also been implicated as a precursor in the formation of long $Mo_6S_3I_6$ NWs.[18] This dual behavior highlights its ambiguous role as both a competitor and a potential stepping stone in nanowire formation. Pure MoI_2 typically forms low-aspect-ratio crystals, and its direct synthesis from elements is complicated by the low reactivity of molybdenum and high iodine pressures that can result in unwanted phases like MoI_3.[19,20]

Sulphur plays a crucial role in modifying the stability and growth pathways of Mo–S–I nanostructures. In compounds such as $Mo_6S_2I_8$, sulphur helps stabilize cluster-based 1D nanowires composed of Mo_6 octahedra coordinated by a mixed shell of inner and apical ligands,[21–23] although its specific effect on phase stability and morphology has not been clear. Similar ideas have been explored in related chalcogenide-halide systems,[24–27] but a clear demonstration in the Mo–S–I family has been missing.

To address this knowledge gap, we demonstrate that trace sulphur incorporation stabilizes a metastable $MoI_{2-x}S_x$ phase, which grows as high-aspect-ratio nanowires in contrast to the low-aspect-ratio prisms of pure MoI_2. This intermediate phase subsequently transforms into $Mo_6S_2I_8$ NWs, revealing a sulphur-promoted growth pathway within the Mo–S–I system. Through comprehensive structural and electronic characterization, we clarify the previously ambiguous role of MoI_2 in nanowire formation and introduce a broader concept: minor compositional tuning can unlock metastable intermediates that serve as templates for controlling nanostructure morphology and function.

2. Experimental section

2.1 Materials and synthesis

The Mo–S–I compound was synthesized from the molybdenum powder (Aldrich, <150 μm, 99.9%), sulphur flakes (Aldrich, <150

---

[a] Jozef Stefan Institute, Jamova cesta 39, SI-1000, Ljubljana, Slovenia. E-mail: anja.pogacnik@ijs.si
[b] Faculty of Mathematics and Physics, Jadranska ulica 19, SI-1000 Ljubljana, Slovenia

μm, 99.99%) and iodine beads (Aldrich, −10 mesh, 99.999%) by one-step chemical vapor transport. 600 mg of Mo, 75.2 mg of S, and 1300 mg of I were inserted into a quartz ampoule that was 20 cm long and 2.5 cm in diameter. The ampoule was evacuated to pressure (10^{-6} mbar) and sealed. The transport reaction took place in a two-zone horizontal furnace for 200 h under a temperature gradient of 5.5 K cm^{-1}. Around 5–10 wt% of the starting material was transported from the hot-temperature zone (1133 ± 5 K) to the low-temperature zone (1010 ± 5 K) of the ampoule.

As a reference, a bulk MoI_2 was synthesized from Mo powder and S flakes in the stoichiometric ratio Mo : I = 1 : 2. The ampoule was evacuated to 10^{-6} mbar and put into the furnace heated to 1010 K for 72 h.

2.2 Characterization methods

2.2.1 X-ray diffraction (XRD). Measurements were performed at room temperature using a Bruker D4 Endeavor diffractometer with a quartz monochromator and $K\alpha_1$ radiation (λ = 0.1541 nm) and a Sol-X energy dispersive detector. The angular range was 6°–73°, with a step size of 0.04° and 4 s per step. Samples were rotated at 6 rpm during data acquisition.

2.2.2 Scanning electron microscopy (SEM) and energy dispersive X-ray analysis (EDS). SEM images were obtained using Thermo Fisher Verios 4G HP with a secondary electron TLD detector. X-ray EDS was performed using an Oxford instruments Aztec Live and Ultim Max SDD 65 mm^2 integrated into the SEM.

2.2.3 Raman spectroscopy. Raman measurements were conducted on a WITec Alpha 300 RS scanning confocal Raman microscope in a backscattered geometry. A polarized Nd:YAG laser operating at wavelengths of 532 nm and 633 nm was focused through a 100×/0.9 objective onto areas smaller than 1 μm^2. Laser power at the sample ranged from 0.3 to 0.9 mW. It was experimentally determined that this is the optimal power for avoiding damage or oxidation of the samples. The samples in the shape of a foil, which grows flat at the interface with quartz substrate and is composed of perpendicularly grown NWs on the top, were prepared either by attaching the NW-side of Mo–S–I compound onto conductive carbon tape to observe the initial growth phase or by dispersing the compound in IPA (99.99%) and drop-casting it on chromium-coated glass substrate.

2.2.4 UV-Vis spectroscopy. Absorbance spectra were recorded using a Shimadzu UV-1650PC UV-Vis-NIR spectrometer. Low-concentration solutions (0.01 mol L^{-1}) were prepared by sonicating the samples in IPA (99.99%) at 120 W. Spectra were acquired in the 200–1100 nm range with 1 nm steps.

2.2.5 Transmission electron microscopy (TEM). Cross-sections of the $MoI_{2-x}S_x$ NWs were obtained using a Helios NanoLab 650 FIB-SEM operating at 10^{-6} mbar. High-resolution TEM (HR-TEM) and electron diffraction (TED) images were obtained using a Cs probe-corrected JEOL ARM 200CF TEM/STEM microscope equipped with a cold-FEG electron source, operating at 200 kV. Atomic distances and angles between rows were analysed using Digital Micrograph software with an accuracy of 0.04 nm and 0.5°, respectively.

2.2.6 STM, AFM, and KPFM. Ultra-high vacuum (UHV) STM, AFM and KPFM measurements were performed on an Omicron UHV VT-AFM (Scienta Omicron, Germany) operating at 3×10^{-9} mbar. KPFM was operated in frequency modulation (FM) mode using NSG 10-Pt (Spectrum Instruments, Russia) or PPP-NCHPt (Nanosensors, Switzerland) tips. Topography and contact potential difference (CPD) were measured simultaneously. Samples were prepared either by attaching the NW-side of the foil to the conductive carbon tape or by dispersing it in IPA (99.99%) and drop-casting them onto epitaxial Au(111) thin film grown on mica substrate (Phasis Sàrl, Switzerland).

The sample work function (ϕ_{SAMPLE}) is given by $\phi_{\text{SAMPLE}} = \phi_{\text{TIP}} + e \cdot V_{\text{CPD}}$, where ϕ_{TIP} is the work function of the probing tip, V_{CPD} is the measured contact potential difference, and e is the elementary charge. Absolute values were calibrated against freshly cleaved highly oriented pyrolytic graphite (HOPG) (SPI Supplies, grade SPI-1, USA) with a stable work function of 4.60 ± 0.05 eV.[28] Topography images were corrected by adjusting the tilt using the Max Flatness Tilt correction in Scanning Probe Image Processor 6.5.7 software.

3. Results

3.1 Topography and crystal growth

The morphology of the transported material provides the first indication of sulphur's crucial role in shaping the Mo–S–I systems. Scanning electron microscopy revealed a highly inhomogeneous foil structure at the quartz interface (Fig. 1a) with porous regions on the back surface (Fig. 1b). Within these regions, nucleation of rectangular MoI_2 crystallites (Fig. 1c) and triangular flakes of MoS_2 (Fig. 1d) growing on planes parallel to the quartz substrate were frequently observed. Pyramidal facets of MoI_2 crystals are also observed inside the pores (Fig. 1e), marking the onset of NW growth. Due to the space confinement in the pores, it is not clear whether these MoI_2 crystals are completely sulphur free, therefore the intermediate growth is labelled as $MoI_{2-x}S_x$, $x < 0.02$. Incorporation of sulphur in traces triggered the change in the growth orientation and formation of high-aspect-ratio NWs, visible in top and side views of the intermediate layer (Fig. 1f–i) instead of the compact prisms typical of pure MoI_2 which formed during unsuccessful synthesis (Fig. S1).[17,18] Diameters of these NWs vary in the range between 100 nm and 300 nm, while their length is up to 20 μm. Because the growth temperature (1010 K) is very close to the melting temperature of MoI_2 (1003 K), some NWs coalesced into bundles (circled in red in Fig. 1g) or platelets (circled in green Fig. 1h).

3.2 Transmission electron microscopy studies

Transmission electron microscopy further clarified the structural evolution of these NWs. Low-magnification images of two-tip shaped NWs deposited on a lacy carbon film reveal pronounced diameter variations along their length (Fig. 2a), indicative of an evolving composition. The diameter of upper

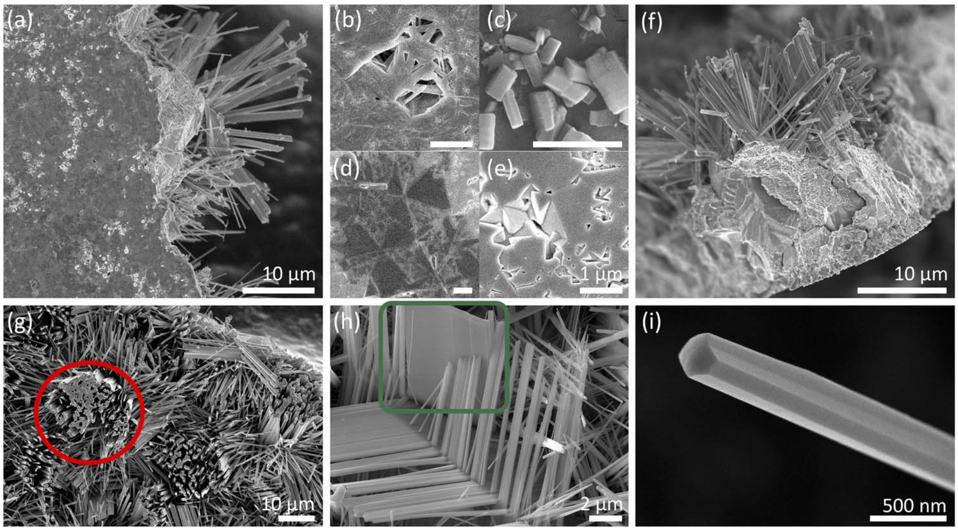

Fig. 1 Scanning electron images of Mo–S–I compound: (a) inhomogeneous structure of foil grown at the interface with quartz, (b) zoom-in on porous structure of the back of the foil, (c) nucleation of MoI_2 crystals as the first stage of growth, (d) triangular shaped MoS_2 flakes as part of the first stage of growth and (e) pyramidal facets of MoI_2 crystals observed inside the holes; (f) a side-view of the intermediate layer; (g) a top-view with NWs; (h) growth of NWs along MoI_2 facets, and (i) the typical shape of NWs. Coalesced nanowires are circled in red (g), and Mo–S–I plates in green (h).

NW is 0.20 µm, and that of the lower one is 0.19 µm. Both NWs underwent a transition during the growth, which abruptly changed their diameters (labelled with *). The lower NW with a long and sharp tip was further investigated near the transition point (A) and close to its tip (B). High-resolution TEM (HRTEM) of the area A reveals a hexagonal distribution of atomic columns (Fig. 2b) grouped into bands consisting of three rows of columns separated by 0.360 nm inside the bands, while the distance between the edge columns of adjacent bands is 0.346 nm, both measured along a row marked with an arrow. The corresponding Fourier Transform (FFT) image (Fig. 2c) yielded patterns consistent with MoI_2, confirming the identity of the intermediate phase. At the end of the same NW (B) (Fig. 2d), HRTEM (Fig. 2e) and FFT (Fig. 2f) analysis revealed the presence of less ordered $Mo_6S_2I_8$ structure, demonstrating a transformation pathway in which the initial $MoI_{2-x}S_x$ NWs gradually convert into $Mo_6S_2I_8$.[29] The observation of split wire tips (Fig. 2d) further supports this phase evolution, suggesting strain release during the transformation.

Cross-section TEM of individual NW embedded in a platinum matrix revealed their internal architecture. The NW displayed a hexagonal cross-section (Fig. 3a), underpinned by

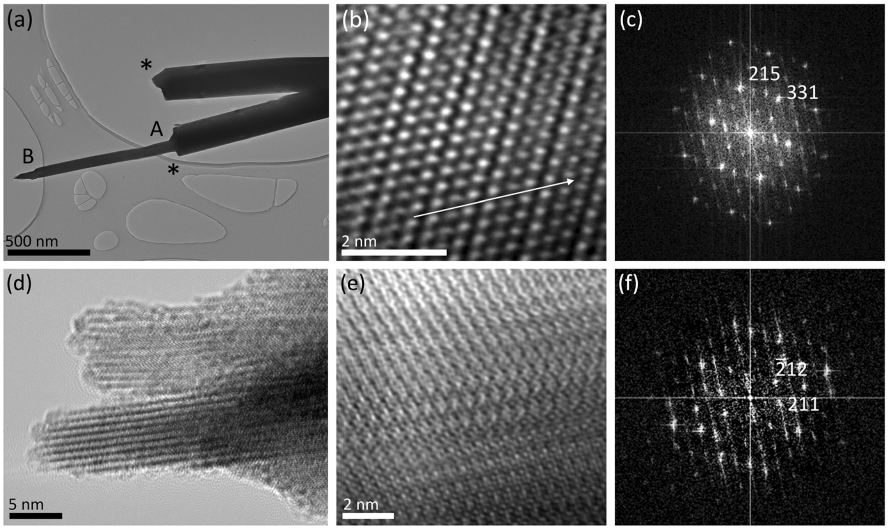

Fig. 2 TEM micrographs of Mo–S–I NWs on a lacy carbon film: (a) transition areas (*) showing changes in diameter; areas A and B were investigated in detail; (b) HRTEM of area A with the NW axis indicated by the arrow and the corresponding (c) FFT image indexed as the $[141\bar{3}\bar{3}]$ zone of the MoI_2 phase; (d) split tip of the NW; (e) HRTEM of area B with the corresponding (f) FFT image indexed as $[3\bar{2}\bar{4}]$ zone of the $Mo_6S_2I_8$ phase.

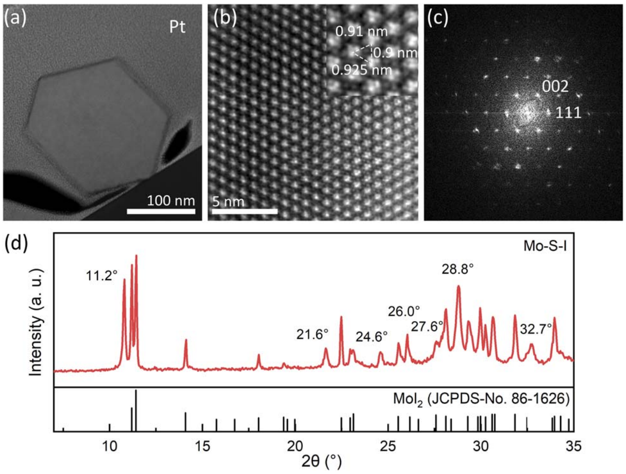

Fig. 3 TEM images of the cross-section of a single MoI$_2$ NW: (a) hexagonal cross-section embedded in a platinum matrix; (b) hexagonal distribution of [Mo$_6$I$_8$] clusters; (c) FFT image indexed along the [1$\bar{1}$0] zone axis of MoI$_2$; (d) XRD pattern of the Mo–S–I compound.

a hexagonal arrangement of [Mo$_6$I$_8$] clusters with distances of 0.9 nm, 0.91 nm, and 0.925 nm between them (Fig. 3b). The FFT image (Fig. 3c) has a hexagonal symmetry with splitting of some peaks, which are attributed to the {113} and {220} interlayer distances of MoI$_2$ in the [1$\bar{1}$0] zone axis, underscoring the structural continuity between the parent and intermediate phases.

3.3 Crystal structure analysis

X-ray diffraction measurements support the findings of TEM analysis (Fig. 3d). Reflections consistent with the orthorhombic MoI$_2$ (JCPDS-No. 86-1626) are dominant (Fig S3 and Table S1), but systematic shifts in peak positions, together with the emergence of additional peaks at 11.2°, 21.6°, 24.6°, 26.0°, 27.6°, 28.8°, 32.7°, and 43.1°, indicated sulphur incorporation and the eventual appearance of the Mo$_6$S$_2$I$_8$ phase.[21,30,31] Crystallographic angles characteristic of Mo$_6$S$_2$I$_8$ are marked above the XRD patterns in Fig. 3d and can also be found in the Table S1. This transported material differs in size and shape from the previously reported non-transported material from the high-temperature zone of the ampoule, where the majority of the material consists of almost pure Mo$_6$S$_2$I$_8$ NWs (Fig. S2).[21,30,31] Together, these observations demonstrate that sulphur stabilizes a metastable MoI$_{2-x}$S$_x$ phase whose structural similarity to Mo$_6$S$_2$I$_8$ allows a smooth transformation pathway.

3.4 Chemical analysis

While narrow NWs, which are in a good electrical and thermal contact with the carbon film or with Pt in the cross-section lamella are relatively stable, thick NWs and Mo–S–I plates are unstable under the electron beam. As an example, a Mo–S–I plate, 1.7 μm in width and about 20 μm in length, immediately started to decompose under the electron beam (Fig. S4). The EDS analysis revealed only around 1 at% of sulphur in this particular plate, indicating that a too low concentration of embedded sulphur does not stabilize the structure of the Mo–S–I irradiated by the electron beam and a strong iodine loss happened during the measurements. The exact sulphur concentration needed for the stabilization is difficult to determine because of the overlap between the L series peaks of Mo and the S Kα peak.

Chemical analysis of NWs revealed that the most commonly observed composition is 7.5% S, 38% Mo and 54.5% I (averaged over 10 sites). The sites with lower percentage of S were also observed: 1.4% S, 33.4% Mo and 65.2% I (averaged over 10 sites). It was noticed that the ratio between S and Mo varies in a range between (0.21 ± 0.04):1, and that in all cases, concentration of Mo relative to the sum of S and I concentrations is very close to the 2 : 1. When measuring the composition on the MoI$_2$ crystals in the foil grown at the interface with quartz, only Mo and I are detected in the ratio of 1 : 2.

3.5 Optical studies

Optical spectroscopy provided complementary insight into this process. UV-Vis absorption spectrum of Mo–S–I compound, which is a mixture of MoI$_2$, MoI$_{2-x}$S$_x$, and Mo$_6$S$_2$I$_8$ NWs, dispersed in IPA, has the highest absorption in the UV region as shown in Fig. 4a (violet line). The absorption peaks are located at 221 nm, 290 nm, 456 nm, and 704 nm, with a weak absorption shoulder visible at around 340 ± 5 nm. These spectral features are consistent with multiple allowed interband electronic transitions arising from the complex electronic structure of Mo–S–I materials, which is governed by hybridized Mo d states and chalcogen/iodine p states, leading to several distinct optical transitions rather than a single absorption edge. For comparative analysis, the absorption spectra of Mo$_6$S$_2$I$_8$ NWs (Fig. S2a) and MoI$_2$ rods (Fig. S2b) are presented together with the spectrum of Mo–S–I compound. UV-Vis absorption spectra (Fig. 4a) show distinct behaviour of different phases: MoI$_2$ prisms exhibited weak absorption, while Mo–S–I compound displayed significantly enhanced absorption across the ultraviolet range. The absorption peaks of Mo–S–I compound closely match those of MoI$_2$, likely reflecting their composition, which is closer to MoI$_2$ than to Mo$_6$S$_2$I$_8$ NWs. Fully transformed Mo$_6$S$_2$I$_8$ NWs showed low absorption in the UV

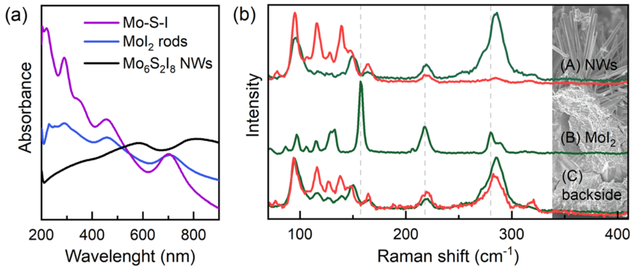

Fig. 4 (a) UV-Vis absorption spectrum of Mo–S–I compound (violet line) compared to Mo$_6$S$_2$I$_8$ NWs (black line) and MoI$_2$ rods (blue line). (b) Typical Raman spectra recorded on Mo–S–I compound composed of MoI$_{2-x}$S$_x$ NWs (A) on pure MoI$_2$ crystals in the middle section of the foil (B), and at the backside of the Mo–S–I compound (C), using 532 nm (green) and 633 nm (red) excitation wavelengths.

region and the highest absorbance at the longest wavelengths of the visible spectrum.

Raman spectroscopy (Fig. 4b), recorded with excitation wavelengths of 532 nm and 633 nm, further confirmed the coexistence of these phases. Spectra from the NWs were similar to those of the overall Mo–S–I foil but exhibited a combination of features from both MoI_2 and $Mo_6S_2I_8$, indicating that the material comprises a mixture of intermediate $MoI_{2-x}S_x$ and $Mo_6S_2I_8$. The positions of the observed Raman shifts are summarized in Table S2.

According to the literature on $Mo_6S_3I_6$,[31] the vibrational modes up to 175 cm^{-1} originate mostly from Mo–Mo vibrations, with the most intense mode is located at 106 cm^{-1}. In the high frequency region, the most intense mode is positioned at 285 cm^{-1} and is attributed to the S–S breathing vibrations.[31] Due to the lack of literature data, pure MoI_2 rods (Fig. S2b) were used to confirm that recorded vibrational modes from the middle section of the Mo–S–I compound correspond to the vibrations of MoI_2.

3.6 Surface and electronic characterization

Electronic characterization highlighted the consequences of this phase evolution. The non-contact atomic force microscopy (nc-AFM) combined with Kelvin probe force microscopy (KPFM) revealed distinct contrast in the contact potential difference (CPD) across the NW cross-section, ~50 nm diameter, deposited on Au(111) substrate (Fig. 5). The CPD image demonstrates for approximately 120 mV lower surface potential at its edges (Fig. 5c), while the average CPD is ~500 mV higher than the value on the Au substrate. Besides on the presented NW, the CPD was measured on several other NWs. The average determined work function (WF) is 5.0 ± 0.1 eV considering the calibration of the AFM tip on HOPG (detailed description in Supplementary Information). The only reference value for comparison is of the $Mo_6S_3I_6$ NWs, where WF of 4.8 ± 0.1 eV was reported.[32]

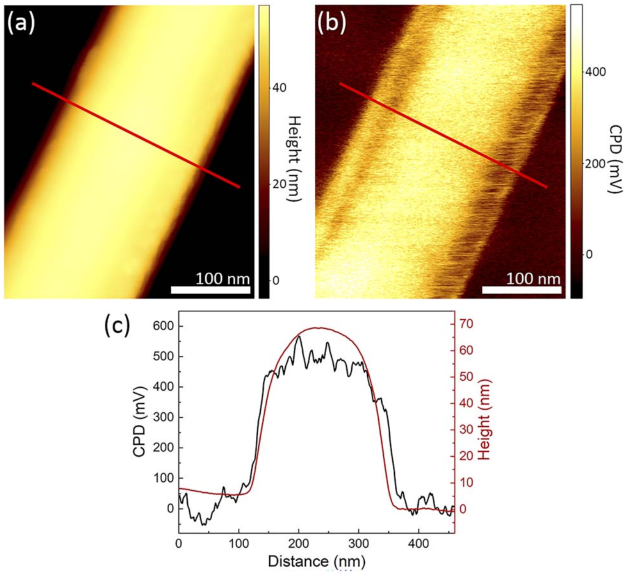

Fig. 5 Mo–S–I nanowire: (a) topography AFM, (b) corresponding CPD image, and (c) line profiles, obtained from the marked red line, averaged over 7 lines.

Since CPD was homogeneous along all measured NWs, it is obvious that the transition from MoI_2 to the intermediate $MoI_{2-x}S_x$ phase or to $Mo_6S_2I_8$ phase was not detected in these randomly selected NWs. High-temperature grown (1133 K) $Mo_6S_2I_8$ NWs (Fig. S2b) provided further evidence of this transition. The nanowire, ~160 nm in diameter, placed on an HOPG substrate was featureless in the topography (Fig. 6a), but a clear transition from a low CPD area to a high CPD area is visible (arrow) in KPFM image (Fig. 6b). The longitudinal termination of this nanowire is rounded (Fig. 6d). This indicates that the nanowire at this end was not torn from the nucleation site and presents the final $Mo_6S_2I_8$ phase of the growth, whereas the low CPD region shows the $MoI_{2-x}S_x$ phase. $MoI_{2-x}S_x$ phase consistently exhibited a lower work function (~4.6 eV), whereas the completely transformed $Mo_6S_2I_8$ phase reached 5.0 eV, demonstrating a substantial modification of surface electronic properties upon sulphur-driven transformation. The average WF value of the measured NWs (Fig. 5) aligns with the $Mo_6S_2I_8$ phase, meaning that during preparation of samples *via* sonification, the NW likely detached from the Mo–S–I foil situated above the intermediate $MoI_{2-x}S_x$ phase. It can be deduced that the $Mo_6S_2I_8$ nanowires are the primary product in the high-temperature area and begin to develop as an intermediate $MoI_{2-x}S_x$ phase, which converts into the $Mo_6S_2I_8$ compound when the partial concentration of iodine decreases due to its embedding into the iodine-rich compound.

The surface potential was also measured on the backside of the Mo–S–I foil with no comparison to the Au substrate in the same scan. CPD was strongly inhomogeneous and varied in the range between 10–300 mV (Fig. S6).

Scanning tunneling microscopy (STM) and spectroscopy (STS) allowed a more detailed analysis of the electronic structure (Fig. 7). Low-magnification STM imaging (Fig. 7a and b) validated the NW morphology, while also displaying a noticeable difference between edges and the middle section of the

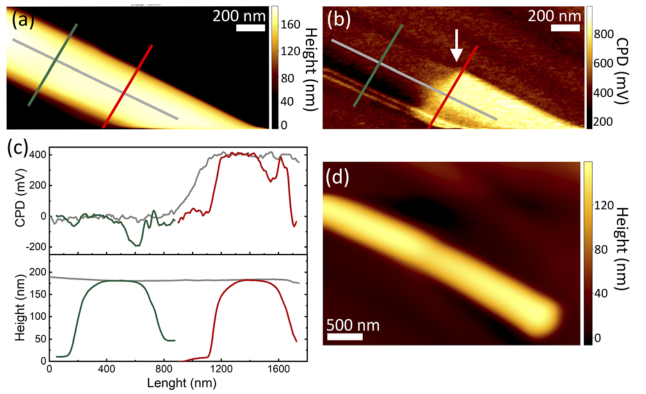

Fig. 6 Nanowire synthesized at the high-temperature zone: (a) nc-AFM image; (b) KPFM image with visible transition from high-CPD to low-CPD areas, and (c) the corresponding line profiles; (d) longitudinal termination of the nanowire.

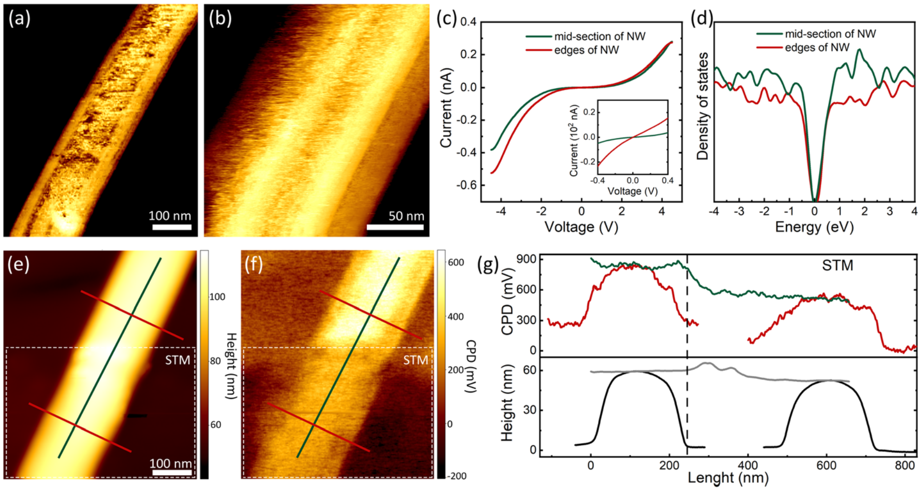

Fig. 7 Mo–S–I nanowire before and after STM scanning: (a) low-magnification STM image (450 mV, 300 pA); (b) zoom-in STM image; (c) averaged *I*–*V* spectra over at least 20 points; (d) density-of-states plots, and after STM scanning: (e) nc-AFM image; (f) KPFM image showing localized reduction of CPD in the scanned area; (g) line profiles of height and CPD along the marked lines in (e) and (f).

NW. The averaged current–voltage (*I*–*V*) curves (Fig. 7c) yielded density-of-states (DOS) plots (Fig. 7d), calculated from $(dI/dV)/(I/V)$. The DOS exhibits a narrow U-shaped gap with $E_g \sim 1$ eV at the edges and ~1.2 eV at the central area of the NW. The apparent "metallic" behavior at the NW edges (Fig. 7c-inset) could arise from an enhanced local density of states associated with surface- or defect-induced states, while the NW centers maintain a semiconducting band gap of ~1.2 eV. This duality is consistent with localized surface conduction coexisting with a semiconducting core.

Subsequent STM scanning locally modified the CPD, as revealed by nc-AFM and KPFM imaging of the same region (Fig. 7e and f) with the STM scan area marked by dashed frames. The KPFM image after the STM scans is shown in Fig. 7e–g. Line profiles (Fig. 7g) indicate a localized height reduction of ~7 nm and a decrease of ~360 mV in the CPD value, but only on the section of the NW that was previously scanned by STM. The CPD of the Au substrate following STM scans also dropped by ~300 mV, likely due to the elimination of contaminants resulting from drop-casting the dispersion onto the substrate. The net CPD change on the NW remains evident (~60 mV). Low-energy electrons in STM in close vicinity of the sample and under a strong electric field gradient could remove surface contamination, similar to 20–30 eV electrons in SEM.[33] Part of these electrons got trapped at the structural defects causing a decrease of work function of the STM-scanned area. Localized reduction in CPD on NW is consistent with electron injection or defect creation, highlighting the dynamic nature of the Mo–S–I NW surface electronic structure.

4. Discussion

A thorough investigation of growth products of a chemical transport reaction involving Mo, S, and I conducted under a temperature gradient, showed the presence of an intermediate $MoI_{2-x}S_x$ phase grown in a nanowire-like form with a hexagonal cross-section. Chemical analysis indicates that the composition of NWs closely resembles MoI_2, although all the nanowires exhibit traces of sulphur. Unlike the well-known orthorhombic MoI_2 structure,[16] which forms rectangular prisms with a small aspect ratio (Fig. 1c), these sulphur-containing NWs grow along the [110] direction consistent with the same MoI_2 structure, maintaining the lattice parameters of MoI_2: $a = b = 1.2562$ nm, and $c = 1.5803$ nm, but creating hexagonal prisms with a high aspect ratio. The presence of sulphur clearly supports the growth in the nanowire-like structure. The quantitative EDS analysis performed on several single NWs showed that the ratio between S and Mo varies in a range between (0.21 ± 0.04):1. Due to the concentration of Mo in relation to the total concentrations of S and I being nearly at the 1 : 2 ratio, and given that the structure can be still characterized by the lattice parameters of MoI_2, one can conclude that part of the iodine in the MoI_2 structure was interstitially substituted by sulphur.

The further alteration of morphology from rectangular prisms of MoI_2 to hexagonal NWs may indicate a change in connections between $[Mo_6I_8]$ clusters. In the orthorhombic MoI_2 structure the adjacent clusters are connected by four apical iodine atoms, whereas in the hexagonal $MoI_{2-x}S_x$ NWs these connections might differ. Currently, it remains unclear which sites (inner or apical) are occupied by sulphur atoms. In comparison to the final phase of the growth, *i.e.* the $Mo_6S_2I_8$ compound structure, where the Mo_6 clusters form chains linked by S and I atoms, S atoms in this intermediate phase may be situated in either apical or inner positions. In contrast to the $Mo_6S_2I_8$ chains, which are coupled solely by VdW forces, the $MoI_{2-x}S_x$ structure remains semi-3D-like, even though the growth direction along the [110] direction already suggests a potential dominance of 1D growth. Because of a high iodine content in the intermediate $MoI_{2-x}S_x$ compound, the $MoI_{2-x}S_x$ NWs form in the beginning of the growth process, when plenty of iodine is still available. As the iodine partial pressure drops due to its consumption in the growth products, the compound of the $Mo_6S_2I_8$ composition becomes dominant, which has a lower Mo–I ratio while also incorporating S. The transition between $MoI_{2-x}S_x$ and $Mo_6S_2I_8$ phases is visible in the TEM micrograph (Fig. 3a), in the corresponding TED patterns (Fig. 2c and f), and in the KPFM image (Fig. 6).

The work function evolution and CPD sensitivity underscore the importance of minor sulphur incorporation in unlocking metastable intermediates as templates for high-aspect-ratio NW growth, providing a generalizable strategy for morphology and property control in cluster-based nanostructures. The stabilization of the $MoI_{2-x}S_x$ phase indicates strong resistance to oxidation under ambient conditions, enabling detailed characterization without the need to maintain the sample in high-vacuum environments.

The sensitivity of the $MoI_{2-x}S_x$ phase to electron irradiation can be attributed to its metastable structure and the loss of iodine from that structure. The final MoO_3 product (Fig. S4b and c) indicates that electron beam breaks down the structure either through thermal effects *via* Coulomb heating or electrically by destabilizing chemical bonds. The structural similarity of intermediate phase and $Mo_6S_2I_8$ facilitates a smooth transformation, while optical absorption, Raman features, and electronic properties evolve in a systematic fashion. This is additional evidence that intermediate phase cannot be explained either by pure MoI_2 structure or final $Mo_6S_2I_8$ product.

5. Conclusion

In this work, we demonstrate a sulphur-promoted growth pathway in the Mo–S–I system, where incorporation of sulphur in traces stabilizes a metastable $MoI_{2-x}S_x$ phase that forms high-aspect-ratio NWs grown from initially nucleated MoI_2 prisms. These NWs, with diameters of 100–300 nm and lengths up to 20 μm, growing at the beginning of the growth process, represent an intermediate phase for the growth of the $Mo_6S_2I_8$ NWs. Comprehensive characterization, including XRD, TEM, SEM, UV-Vis, Raman, AFM/KPFM, and STM/STS, reveals that sulphur not only stabilizes the intermediate morphology but also modulates the electronic properties, giving rise to a U-shaped band gap of ~1.2 eV in the NW cores while maintaing enhanced edge conductivity. Work function measurements further highlight the tunability of surface electronic properties along the NWs, with a sharp transition marking the growth front.

These findings clarify the dual role of MoI_2 as both a precursor and a transient structure in the formation of functional Mo–S–I NWs and underscore the significance of minor compositional tuning in accessing metastable intermediates. The concept of sulphur-stabilized intermediates provides a generalizable strategy for controlling nanowire morphology, phase evolution, and electronic properties in cluster-based systems. This work opens avenues for the rational design of Mo–S–I nanostructures for applications in optoelectronics, nanoelectronics, and composite materials.

Author contributions

A. Pogačnik Krajnc: conceptualization, methodology, data curation, formal analysis, investigation, writing – original draft, writing – review & editing. J. Jelenc: investigation, methodology, formal analysis, writing – review & editing. L. Pirker: investigation, writing – review & editing, S. D. Škapin: investigation, M. Remškar: conceptualization, data curation, methodology, investigation, formal analysis, writing – original draft, writing – review & editing, supervision.

Conflicts of interest

There are no conflicts to declare.

Data availability

All data relevant to this article are provided either within the main manuscript or in the supplementary information (SI). The raw data from the experiments that formed the basis of this paper have been stored in the Zenodo digital archive, accessible through the following link: The datasets are available: https://doi.org/10.5281/zenodo.17746847. Supplementary information is available. See DOI: https://doi.org/10.1039/d5na01101a.

Acknowledgements

This work was supported by the Slovenian Research and Innovation Agency (PR-09761).

References

1 A. Meden, A. Kodre, J. Padežnik Gomilšek, I. Arčon, I. Vilfan, D. Vrbanic, A. Mrzel and D. Mihailovic, *Nanotechnology*, 2005, **16**, 1578.
2 J. Karthikeyan, V. Kumar and P. Murugan, *J. Phys. Chem. C*, 2015, **119**(24), 13979–13985.
3 D. Mandrino, D. Vrbanic, M. Jenko, D. Mihailovic and S. Pejovnik, *Surf. Interface Anal.*, 2008, **40**, 1289–1293.
4 M. Žumer, V. Nemanič, B. Zajec, M. Remškar, M. Ploscaru, D. Vengust, A. Mrzel and D. Mihailović, *Nanotechnology*, 2005, **16**, 1619.
5 M. Rangus, M. Remškar and A. Mrzel, *Microelectron. J.*, 2008, **39**, 475–477.
6 A. Majkić, C. Gadermaier, N. Celic, P. Topolovsek, G. Bratina and D. Mihailovic, *Sol. Energy Mater. Sol. Cells*, 2014, **127**, 63–66.
7 G.-S. Kang, Q. Hu, S. Li, S. V Bhoraskar and J.-B. Yoo, *Mater. Res. Express*, 2022, **9**, 085502.
8 P. Topolovsek, C. Gadermaier, D. Vengust, M. Strojnik, J. Strle and D. Mihailovic, *Nano Lett.*, 2015, **15**(2), 813–818.
9 S. J. Chin, P. Hornsby, D. Vengust, D. Mihailović, J. Mitra, P. Dawson and T. McNally, *Polym. Adv. Technol.*, 2012, **23**, 149–160.
10 M. Huskić, A. Sever-Škapin, D. Vengust and D. Mihailović, *Composites, Part B*, 2014, **56**, 62–67.

11 J. H. Park, H. Jo, C.-Y. Seong, K. H. Kim, A. Mrzel, G. Scalia and Y. W. Park, *Phys. Status Solidi A*, 2014, **211**, 1122–1127.

12 J. Casanova-Chafer, R. Garcia-Aboal, P. Atienzar, M. Feliz and E. LIobet, *ACS Appl. Mater. Interfaces*, 2022, **14**(51), 57122–57132.

13 R. Zhang, M. Hummelgård, D. Dvorsek, D. Mihailovic and H. Olin, *J. Colloid Interface Sci.*, 2010, **348**(2), 299–302.

14 M. Devetak, B. Berčič, M. Uplaznik, A. Mrzel and D. Mihailovic, *Chem. Mater.*, 2008, **20**(5), 1773–1777.

15 Handbuch der Präparativen Anorganischen Chemie, 3., Umgearbeitete Auflage. Band III, Ferdinand Enke, Stuttgart, 1981, 1539.

16 Z. G. Aliev, L. A. Klinkova, I. V. Dubrovin and L. O. Atovmyan, *Zh. Neorg. Khim.*, 1981, **26**, 1964–1967.

17 D. Dvorsek, M. Zumer, V. Nemanic, D. Mihailovic and D. Vengust, *J. Appl. Phys.*, 2007, **102**(11), 114308.

18 S. Oh, S. Chae, K. H. Choi, B. J. Kim, S. H. Lee, C. Wang, Z. Liu, J. Jeon, J.-H. Lee, H. K. Yu and J.-Y. Choi, *J. Alloys Compd.*, 2019, **803**, 499–504.

19 J. Lewis, D. J. Machin, R. S. Nyholm, P. Pauling and P. W. Smith, *Chem. Ind.*, 1960, 259.

20 M. Ströbele, R. Thalwitzer and H. Jürgen Meyer, *Inorg. Chem.*, 2016, **55**(22), 12074–12078.

21 M. Viršek, M. Krause, A. Kolitsch, A. Mrzel, I. Iskra, S. D. Škapin and M. Remškar, *J. Phys. Chem. C*, 2010, **114**(14), 6458–6463.

22 A. P. C. Perrin, *Eur. J. Inorg. Chem.*, 2011, 3848–3856.

23 M. Viršek, N. Novak, C. Filipič, P. Kump, M. Remškar and Z. Kutnjak, *J. Appl. Phys.*, 2012, **112**, 103710.

24 Y. K. Chung, W. G. Lee, S. Chae, J. Y. Choi and J. Huh, *Sci. Rep.*, 2019, **9**, 1222.

25 M. Zhang, F. Grasset, Y. Masubuchi, T. Shimada, T. K. N. Nguyen, N. Dumait, A. Renaud, S. Cordier, D. Berthebaud, J.-F. Halet and T. Uchikoshi, *Nanomaterials*, 2023, **13**, 478.

26 J. Yu, X. Chen, Y. Wang, H. Zhou, M. Xue, Y. Xu, Z. Li, C. Ye, J. Zhang, P. A. van Aken, P. D. Lund and H. Wang, *J. Mater. Chem. C*, 2016, **4**, 7302–7308.

27 J. H. Kim, D. H. Ryu, S. H. Jm, J. Jeong and C. E. Song, *Microstructures*, 2025, **5**, 2025063.

28 W. N. Hansen and G. J. Hansen, *Surf. Sci.*, 2001, **481**(1–2), 172–184.

29 M. Remškar, A. Mrzel, M. Viršek and A. Jesih, *Adv. Mater.*, 2007, **19**, 4276–4278.

30 M. Remškar, A. Mrzel, M. Virsek, M. Godec, M. Krause, A. Kolitsch, A. Singh and A. Seabaugh, *Nanoscale Res. Lett.*, 2011, **6**(1), 1–6.

31 J. M. Todorović, Z. D. Dohčević-Mitrović, D. M. Đokić, D. Mihailović and Z. V. Popović, *J. Raman Spectrosc.*, 2010, **41**, 978–982.

32 M. Strojnik, A. Omerzu, A. Majkić, P. M. Mihailovic, J. Lukan, G. Bavdek, G. Bratina, D. Cvetko, P. Topolovsek and D. Mihailovic, *Langmuir*, 2011, **27**(8), 4296–4299.

33 L. Frank, E. Mikmeková and M. Lejeune, *Appl. Surf. Sci.*, 2017, **407**, 105–108.